UC Santa Barbara
UC Santa Barbara Previously Published Works

Title
MEMS device for applying shear and tension to an epithelium combined with fluorescent live cell imaging

Permalink
https://escholarship.org/uc/item/4405q6wb

Journal
Journal of Micromechanics and Microengineering, 30(12)

ISSN
0960-1317

Authors
Garcia, Miguel A
Sadeghipour, Ehsan
Engel, Leeya
et al.

Publication Date
2020-12-01

DOI
10.1088/1361-6439/abb12c

Peer reviewed

MEMS device for applying shear and tension to an epithelium combined with fluorescent live cell imaging

Miguel A Garcia[#1,2], **Ehsan Sadeghipour**[#3,4], **Leeya Engel**[3,4,5], **W James Nelson**[1], **Beth L Pruitt**[6,7,8]

[1]Department of Biology, Stanford University, Stanford, CA 94305, United States of America

[2]Department of Neurosurgery, Stanford University, Stanford, CA 94305, United States of America

[3]Department of Mechanical Engineering, Stanford University, Stanford, CA 94305, United States of America

[4]Department of Bioengineering, Stanford University, Stanford, CA 94305, United States of America

[5]Department of Chemical Engineering, Stanford University, Stanford, CA 94305, United States of America

[6]Department of Mechanical Engineering, University of California, Santa Barbara, CA 93106, United States of America

[7]Department of Biomolecular Science and Engineering, University of California, Santa Barbara, CA 93106, United States of America

[8]Department of Molecular, Cellular and Developmental Biology, University of California, Santa Barbara, CA 93106, United States of America

[#] These authors contributed equally to this work.

Abstract

Mechanical forces play important roles in the biological function of cells and tissues. While numerous studies have probed the force response of cells and measured cell-generated forces, they have primarily focused on tensile, but not shear forces. Here, we describe the design, fabrication, and application of a silicon micromachined device that is capable of independently applying and sensing both tensile and shear forces in an epithelial cell monolayer. We integrated the device with an upright microscope to enable live cell brightfield and fluorescent imaging of cells over many hours following mechanical perturbation. Using devices of increasing stiffness and the same displacement input, we demonstrate that epithelia exhibit concomitant higher maximum resistive tensile forces and quicker force relaxation. In addition, we characterized the force response of the epithelium to cyclic shear loading. While the maximum resistive forces of epithelia under cyclic shear perturbation remained unchanged between cycles, cyclic loading led to faster relaxation of the resistive forces. The device presented here can be applied to studying the force response of

blp@ucsb.edu .

other monolayer-forming cell types and is compatible with pharmacological perturbation of cell structures and functions.

Keywords

MEMS; shear; tension; mechanobiology; live cell imaging; cyclic shear loading; epithelial cell monolayer

1. Introduction

Cells in biological systems sense each other and their surrounding environment by chemical, electrical, and mechanical means. The machinery, structures, and forces used by cells to mechanically interact with each other have been studied using a variety of engineered devices of increasing complexity that include wrinkling polymer substrates (Harris *et al* 1980), traction force microscopy (Plotnikov *et al* 2014, Ribeiro *et al* 2016), atomic force microscopy (AFM) (Taubenberger *et al* 2014), and engineered silicon-based force sensors and actuators (Mukundan *et al* 2013); see Roca-Cusachs *et al* for a comprehensive review on quantifying forces in cell biology (Roca-Cusachs *et al* 2017).

Silicon tools for studying cell mechanics are typically more expensive to fabricate than polymer tools, but generally enable more precise and repeatable application and measurement of mechanical perturbation. AFM and other methods based on the deflection of silicon micromachined cantilevers have become widely adopted for studying the physical properties of a range of biological systems, from single proteins to small animals, including the nematode *C elegans* (Lee *et al* 2007, Petzold *et al* 2011, Doll and Pruitt 2012). Other silicon tools have utilized folded flexures for in-plane perturbation of cells (Sun *et al* 2002, Siechen *et al* 2009).

Measuring the mechanical properties of single cells has provided insights into the biophysical aspects of cellular processes such as adhesion, migration, and cell contraction (Mukundan *et al* 2009, 2009, 2013, Sochol *et al* 2011, Maitre *et al* 2012, Hui and Pang 2019). However, cellular mechanical properties within an integrated multicellular system, such as an epithelial cell monolayer, remain poorly understood. This knowledge would greatly benefit our understanding of tissue homeostasis and how tissues respond to forces of different magnitudes during disease and development.

We recently studied the effects of shear perturbation on a Madin-Darby canine kidney (MDCK) cell epithelium using a novel MEMS device (Sadeghipour *et al* 2018). This device applied shear to an epithelium of thousands of cells. Upon one-time shear at the mid-line of an epithelial monolayer, we observed local, short-term deformations of 2–3 cell layers, and long-term collective oscillatory movements in all cells. This behavior initiated at the shear plane, spread away from it, and then dampened. This work revealed that local deformation of a few cells by shear generates a mechanical signal that is relayed to the rest of the epithelium through tension developed by actomyosin contraction linked to E-cadherin cell–cell adhesion. While the device used in that study revealed the effects of a single in-plane shear event, we sought to modify the device to test other physiologically relevant forms of

mechanical perturbations, e.g. tension and cyclic shear. Here, we describe the design and fabrication of MEMS devices with different spring designs; using a fixed displacement, these different spring stiffnesses translate into varied forces applied to a cell monolayer. Additionally, these devices are designed to apply tensile and shear forces independent of each other, allowing us to study the decoupled response of MDCK cell epithelia to the application of different amounts of tension, and to cyclic shear. Measurements were performed to demonstrate the functionality of the device design for all of these studies. The mechanical properties and behaviors of cells that can be derived from these studies can provide deeper insights into tissue biology.

2. Design and fabrication

2.1. Design specifications

The design of the cell mechanics device was guided by three requirements: (1) Apply 100 μm of in-plane shear (X) and 50 μm of tensile (Y) displacement to a sheet of MDCK cells; (2) Simultaneously sense the X and Y forces across the monolayer with minimal off-axis crosstalk; and (3) Allow 48 h of upright brightfield and fluorescence live cell imaging microscopy of the cells. These displacement ranges were selected to be physiologically relevant and also large enough to induce changes in the behavior of cells, *i.e.* deformations of greater than 2–4 cell lengths for MDCK cells (~15 μm in a confluent monolayer). This is consistent with previous studies where applied stretch of 2–3 cell lengths elicited observable changes in an E-cadherin tension sensor (Borghi *et al* 2012).

These actuation, microscopy and metrology requirements translate to device stiffness constraints. For example, the flexures or springs should have stiffnesses similar to that of the monolayer (~1 N m^{-1}) (Sadeghipour *et al* 2018) and an order of magnitude stiffer out-of-plane. These constraints minimize out-of-plane motion and cross-talk, and keep the epithelium in optical focus even for the small depth of field of a high magnification objective. The elastic properties of silicon further provide stability over tens of hours of live cell microscopy. Furthermore, the device had to be compatible with cell culture media, an aqueous solution containing salts, amino acids, and lipids. Keeping the cell culture medium at a constant molarity while performing long experiments is addressed in greater length in the Deployment and Testing section.

2.2. Device design

2.2.1. Form and function—Figure 1(a) shows a functional device that was fabricated from a silicon on insulator (SOI) wafer by patterning both the 50 μm device layer and the 400 μm handle layer. It was diced using a laser cutter and released by etching the buried oxide (BOX) layer. Following treatment with an extracellular matrix (ECM) protein, the device can be used for cell mechanics experiments. The device consists of an actuating side and a sensing side (figure 1(a)). The actuating component is a spring-loaded 250×1000 μm silicon cell adhesion plank that is moved at μm-scale resolution using a tungsten needle attached to a three-axis micromanipulator (Newport). Measuring the movement of the other spring-loaded silicon cell adhesion plank using live cell microscopy allows in-plane forces to be sensed in both the tensile and shear directions. Silicon folded flexures are used as springs

in this design. Four folded flexures suspend each cell adhesion plank for tensile loading, while an additional and independent four flexures suspend the plank in the shear direction.

The two cell adhesion planks can be actuated in either in-plane direction to produce and sense tension, or shear in an epithelium adhered to the top surface (figure 1(b)). The planks are fabricated with a 5 μm gap between them. This gap is large enough to allow photolithography and deep reactive ion etching (DRIE) to define the silicon features. When brought together, the two cell adhesion planks form a single 500×1000 μm platform for cell mechanics experiments. This platform can support 5000 to 10000 MDCK cells depending on the level of monolayer density. All of the moving parts are defined using a single mask step and DRIE process (figure 1(c)).

2.2.2.   Mechanical design.—Two sets of four folded flexures are responsible for suspending and enabling the movement of each half of the device independently in tension and in shear (figure 1(a)). The inner flexures enable independent motion of each plank in shear (X), while the outer flexures enable independent motion in the tensile (Y) direction. We model the flexures as spring equivalents using beam theory and superposition. By symmetry, either half of the device can be actuated while displacement of the other half can be monitored to infer force across a monolayer of cells.

Each shear folded flexure comprises three springs in series, with four folded flexures in parallel providing the overall shear stiffness for one plank. Equation (1) describes the overall shear stiffness of each half of the device, where E is the Young's modulus, t is the thickness of the wafer device layer, w is the width of each flexure, L_{S1} ($L_{S1} = L_{S3}$) is the length of the two outside beams, and L_{S2} is the length of the middle beam. The effective Young's Modulus for to the flat of a silicon (100) wafer is 169 GPa (Hopcroft *et al* 2010).

$$
\begin{aligned}
k_S^{-1} &= \frac{L_{S1}^3}{4Etw^3} + \frac{L_{S2}^3}{4Etw^3} + \frac{L_{S3}^3}{4Etw^3} \\
k_S &= \frac{4Etw^3}{2L_{S1}^3 + L_{S2}^3} .
\end{aligned}
\tag{1}
$$

Each tension folded flexure comprises four springs in series, with four folded flexures in parallel providing the overall tensile stiffness. Equation (2) describes the overall tensile stiffness of each half of the device, where L_T is the length of the beams.

$$
k_T = \frac{Etw^3}{L_T^3} .
\tag{2}
$$

Table 1 lists the design values for k_S and k_T in equations (1) and (2). The width of the folded flexures was varied (5, 8, or 11 μm) to achieve different levels of device stiffness. By varying device stiffness, an epithelium spanning the two cell adhesion planks can be subjected to different force levels for the same level of actuator displacement. Thus, force and displacement can be independently varied between experiments. Table 2 lists the shear and tensile stiffness of the device for the different widths of folded flexures. In addition,

table 2 shows the force resolution (F_{min}) measured with the sensor ($F = kx$, where x is pixel length) for each device type when using a 10X air (1.54 pixel μm^{-1}) objective and a Hamamatsu Orca-R2 camera to measure the displacement of the sensor. Device design stiffness was calculated using established analytical models (Liu 2005; Kaajakari 2009).

These models assume that spring anchor movements are negligible and spring deformations are primarily one dimensional. In practice, non-ideal deformations in the spring suspensions create offset errors in spring constant calculations. Moreover, fabrication (mask alignment, etch process variability, etc) tolerances contribute to uncertainties of more than 20% in estimation of effective spring constants in silicon beams (Barlian *et al* 2007, Kim *et al* 2011). In this work, we intentionally designed the devices and experiments to apply relative differences in displacements and forces, however, appropriate calibration would be needed to report absolute force with precision greater than 20%–40% (Langlois *et al* 2007, Higgs *et al* 2013). The experiments reported here are based on relative force differences using devices fabricated simultaneously on the same wafer so that they experience the same spring constant offsets; moreover, these offset errors do not affect the biological findings. We compared biological results using devices from the same wafers and operated on the same apparatus to minimize offset errors.

We use equation (3) (Anderson 1994) to estimate the precision of k_S and k_T using the expected uncertainties in the target parameters. In this equation, R represents the dependent variable (k_S or k_T), x is the independent variable, and ω is the uncertainty associated with each variable ($\omega_L = 1 \mu m$, $\omega_w = 1 \mu m$, $\omega_t = 1 \mu m$, $\omega_E = 8.45$ GPa).

$$\omega_R = \left[\left(\frac{\partial R}{\partial x_1} \omega_1 \right)^2 + \left(\frac{\partial R}{\partial x_2} \omega_2 \right)^2 + \cdots + \left(\frac{\partial R}{\partial x_n} \omega_n \right)^2 \right]^{1/2}. \tag{3}$$

Table 3 presents the nominal stiffness and uncertainty range of each of the three designs using this analysis. Varying the width of the folded flexures allowed us to vary the stiffness of the devices by an order of magnitude, and even without direct calibration of each device, the expected stiffness ranges for the three designs do not overlap so that the relative comparison between the type and range in loading still provides robust results between treatments and the unloaded controls. We conducted our biological experiments described here using the two stiffer designs, which are also more precise relative to their designed value.

2.3. Fabrication

The devices were fabricated using a two-mask fabrication process (figure 2) and double-polished 100 mm SOI wafers (Ultrasil Corporation, Hayward, CA). These wafers had a device layer thickness of $50 \pm 1 \mu m$, BOX layer thickness of $5 \mu m \pm 5\%$, and a handle layer thickness of $400 \pm 25 \mu m$. The (100) silicon device and handle layers had p-type background doping (Boron, < 0.05 ohm-cm).

The frontside mask (figure 2(a); positive photoresist, digital data dark) defined the features of the device layer including the springs and cell adhesion planks. The backside mask

(figure 2(a); positive photoresist, digital data clear) defined the backside openings in the handle layer. The devices and the opening, an 80-μm wide trench around the cell adhesion planks and the adjacent flexures, were etched into the silicon using a DRIE process. The devices were then released by etching away the BOX layer, where the entire area defined by this trench fell away to reveal a large opening in the handle layer. The large opening was important for five reasons: (1) The device could become inoperable, or at least defective, if any cells adhered between the device and handle layers during the cell deposition process. Removing this piece below the moving parts adjacent to the cells reduced the chances of such a failure mode; (2) These openings allowed us to manipulate the device both from the top and bottom, which increased the uses of the devices, including the possibility of inverting them as part of an inverted microscopy setup; (3) This piece acted as a test structure to time the BOX release. When the piece fell away, the BOX was sufficiently etched and the device was fully released; (4) Instead of etching away this entire region in the DRIE process, we avoided heavily loading the DRIE etch and achieved a large opening with a much smaller and more uniform trench etch; and (5) Keeping a larger handle area intact until the BOX etch made the handling easier because it is more robust.

After marking and cleaning the SOI wafers (figure 2(b)), we annealed them for 16 h at 1100 °C (Thermco Systems; West Sussex, UK) to reduce any residual stress in the thick BOX layer. We cleaned the wafers again (Piranha bath for 20 min., followed by 50:1 HF bath for 10 min. to remove residual oxide), dehydrated them in a 'singe' oven at 150 °C, and treated with an hexamethyldisilazane adhesion promoter. The device layer was spin coated with 1.0 μm of Shipley 3612 photoresist (Dow Chemical; Midland, MI), and photopatterned the resist (KarlSuss MA6 contact aligner, Suss Microtec; Munich, Germany). The 50 μm device layer was etched using DRIE (2.1 μm min^{-1}, Surface Technology Systems; Newport, UK—Bosch Process: Etch: SF6 flow 12 s at 130 sccm; RF coil 600 W; automatic pressure control (APC) valve: 69%; RF Platen 120 W at 13.56 MHz—Passivation: C4F8 flow 7 s at 85 sccm; APC valve: 69%; RF Coil 600 W; RF Platen 0 W—Platen Temperature: 18 °C; Coil Temperature: Not Controlled) (Ayón 1999). We previously found that it was difficult to remove the polymers deposited by the DRIE process during the passivation step, and these polymers often interfered with the proper operation of the device. Thus, we aggressively removed the plasma treated photoresist using: a 30 min. O_2 plasma treatment, a 30 min bath of Remover PG (Microchem; Newton, MA) at 80 °C, a 30 min bath of Dynastrip DL9150 heated to 70 °C, and finally a Piranha bath (20 min.) to thoroughly remove residual DRIE polymers.

The frontside features of the device layer were protected during the subsequent backside etch by coating them with 1.0 μm of low temperature oxide (LTO) at 400 °C in a Tylan low pressure chemical vapor deposition furnace (Tystar Corporation; Garden Grove, CA). The frontside LTO was protected with two coatings of 10 μm SPR 220–7 photoresist (Microchem; Newton, MA), and the backside LTO was removed by placing the wafers in a 6:1 buffered oxide etch (BOE) for 4 min. The frontside resist was removed using a Piranha bath (20 min), and the wafers were prepared with the same pre-lithography steps as explained previously for coating the backside with 7.0 μm of SPR 220–7. The thick photoresist was allowed to degas overnight, and was then exposed with the backside mask (figure 2(a)), and finally developed. The backside was patterned using DRIE (2.1 μm min^{-1}.)

to etch through the 400 μm handle layer. The photoresist and DRIE polymers were removed as explained previously.

The devices were puddle coated with a layer of protective SPR 220–7 photoresist and the devices were diced using a laser cutter. The laser partially burns the photoresist and necessitates a multi-step removal process involving, sequentially, a 20 min O2 plasma treatment, an organic solvent treatment (acetone, methanol, and isopropanol), followed by a 30 min bath of Remover PG at 80 °C. Finally, the BOX layer and the individual devices were released in 6:1 BOE, stopping the etch when the backside island fell away (~10 h).

3. Deployment and testing

3.1. Device preparation

To sterilize newly fabricated devices before cell seeding, we rinsed them twice in 70% ethanol for 5 min, and then twice in MilliQ water for 5 min. We stored devices in MilliQ water prior to use, or in 70% ethanol for longer term storage. When devices were to be dried for storage, we did so in a critical point dryer to prevent flexure collapse from surface tension. We rinsed devices twice in 0.01% acetic acid for 5 min prior to coating (incubation) with ECM protein collagen type 1 (Corning, 354236; 50 μg ml^{-1} diluted in 0.01% acetic acid) for 1 h at room temperature under sterile conditions. Collagen provides a strongly adhesive surface for MDCK cells on silicon.

Following collagen coating, each device was placed in Dulbecco's Modified Eagle Medium (DMEM) low-glucose (200 mg l^{-1}, nutrients and amino acids) medium supplemented with 10% fetal bovine serum (FBS, nutrients and growth hormones) and 1 g l^{-1} sodium bicarbonate (pH buffer), penicillin (30 μg ml^{-1}, antibiotic), kanamycin (1 mg ml^{-1}, antibiotic), and streptomycin (30 μg ml^{-1}, antibiotic). For fluorescence imaging, phenol red (pH buffer) was left out of the culture media in order to reduce background fluorescence. Further, since we use an open-air system, the imaging medium was supplemented with 50 mM HEPES to maintain a neutral pH.

We loaded each device into a 35 mm polystyrene culture dish, which was held in position during actuation with a custom-designed 3D-printed acrylonitrile butadiene styrene plastic holder (figure 3). The dish was placed on the microscope's automated stage, and its position was stabilized with double-sided tape. The cell adhesion planks of the device were manipulated using a 5 μm tip tungsten needle, with the tip (Signatone, SE-T) bent vertically with respect to the silicon device layer attached to a three-axis micromanipulator (Newport Corp., UMR8.25) (figure 3, left).

We were typically able to reuse devices for 5–8 experiments, *i.e.* for as long as they remained undamaged after use and cleaning. After each experiment, devices were treated with collagenase (Sigma-Aldrich, C0130) at a concentration of 2.4 g ml^{-1} for 30 min at 37 °C to remove the collagen coating. The devices were rinsed twice in MilliQ water for 5 min, soaked in 8.25% bleach for 48 h, and rinsed in MilliQ water twice for 5 min at room temperature. Finally, the devices were soaked in 70% ethanol for 3 h, rinsed in MilliQ water

twice for 5 min, and rinsed in 0.01% acetic acid twice for 5 min. The devices were then ready to be functionalized for a new experiment.

3.2. Test setup

Devices were designed with a 5 μm gap between the cell adhesion planks (figure 4(a)). This gap was closed with the micromanipulator before cell seeding (figure 4(b)). This closed position ensured that the cells would form a single monolayer over the 2 adhesion planks.

We used MDCK type GII cells stably expressing E-cadherin:DsRed (MDCK Ecad:DsRed) to visualize the boundaries between cells in all experiments. Prior to seeding, the cells were cultured at 37 °C and 5% CO_2 in DMEM low-glucose (200 mg l^{-1}) media supplemented with 10% fetal bovine serum (FBS), 250 $\mu g\,ml^{-1}$ G418, 1 g l^{-1} sodium bicarbonate, penicillin, kanamycin and streptomycin (PSK). Cell monolayers at 80% confluence were dissociated with trypsin-EDTA (0.05%) (Life Technologies, 25 300–062) for 6 min at 37 °C. Cells were then resuspended at a concentration of 1.5×10^6 cells mL^{-1} in low-calcium (5 μm Ca^{++}) DMEM. The low-calcium temporarily blocks cell–cell adhesion during delivery of cells onto the adhesion planks, which were submerged in DMEM with normal calcium (1.8 mM Ca^{++}) to induce cell–cell adhesion resulting in a uniform and dense cell layer.

We deposited approximately 2700 cells on the closed cell adhesion planks through a glass capillary tube with an inner diameter of 500 μm attached to the tip of a Ramin p10 turn-dial micropipette connected to a separate micromanipulator (figure 4(c)–e). The open dish was sealed with 3 ml of mineral oil to prevent media evaporation during the experiment. After 1 h, the media was agitated gently with an additional ml of media and a micropipette to remove non-adherent cells (figure 4(f)).

3.3. Imaging

Cells were imaged on a Leica DM-RXA2 microscope and a Hamamatsu Orca-R2 camera housed in a customized black acrylic incubator box maintained at 37 °C with an Air-Therm ATX. The entire cell monolayer was imaged using a Leica Fluor 5X objective and selected regions using a Leica Flour 10X objective for all sensing experiments. Prior to the application of shear or tension, the monolayer was imaged for 15 min at 30 s intervals. MDCK E-cad-DsRed cells were imaged in bright field (figure 5, BF) and fluorescence (figure 5, FL), and images were captured during sensing experiments at 200 ms intervals, binning by 2×2 for a final resolution of 2.12 pixels μm^{-1}. Immediately following shear or tension, images were captured every 30 s for 30 min, and then every 5 min for 1.5 h. Images were compiled into stacked files, rotated to horizontally align the planks and then matched to the first image using the Fiji Template Matching plugin. Images were 468×390 pixels.

For shear application experiments, the actuating plank was displaced 100 μm in the X direction and held in that position for the duration of the experiment. This displacement caused in-plane shear deformation at the mid-plane of the monolayer (figure 5, Shear). For tension application experiments, the actuating plank was displaced 50 μm in the Y direction and held in that position for the duration of the experiment. This displacement caused tensile stretch at the mid-plane of the monolayer (figure 5, Tension). To ensure uniform shear or tensile load, for every application of shear and tension we looked for rotation of the cell

adhesion planks. We did not observe any rotation when applying tension or shear. The rate of shear and tension displacement was approximately 20 μm/second. Neither 100 μm shear nor 50 μm tension ruptured individual cells, cell–cell adhesions, or the cell monolayer as a whole (figure 5, Shear + Tension).

To test the device's compatibility with high resolution fluorescence microscopy, cells were imaged using a water immersion 63X objective focused at the cell adhesion plank junction (cell monolayer midline) prior to shear or tension (figures 6(a) and c). Images of MDCK E-cad-DsRed cells revealed easily discernible cell boundaries. Note that under 100 μm of shear, cells at the midline deformed in the direction of shear, but did not rupture (figure 6(b)). Similarly, cells under 50 μm tension at the midline were deformed and were suspended over the open gap between the cell adhesion planks, and did not rupture (figure 6(d)).

From top to bottom, silicon planks are imaged in a closed position, with 100 μm shear displacement, with 50 μm tension displacement, and with both shear and tension. From left to right, the devices are imaged without and with MDCK E-cadherin:dsRed cells in brightfield (BF) and fluorescence (FL).

3.4. Force sensing

The two independently movable cell adhesion planks allowed us to apply tension or shear to the epithelium and to simultaneously sense the resulting force across the monolayer on the other flexure. Tension was applied to the epithelium by moving the actuating plank in the positive Y direction; because the planks are coupled through the monolayer, this also moved the sensing plank in the same direction (figure 7(a)). At each time point the tensile force on the epithelium was calculated as the product of the nominal tensile stiffness (k_T) and the sensor displacement in Y (d_Y). Shear was applied to the epithelium by moving the actuation plank in the positive X direction, which also moved the sensing plank in the same direction (figure 7(b)). At each time point the shear force on the epithelium was calculated as the product of the nominal shear stiffness (k_S) and the sensor displacement in X (d_X). The potential additional force from minimal bending of opposing springs or any other structures would be orders of magnitude smaller than what we are detecting in our shear and tension experiments.

4. Results and discussion

4.1. Tension loading

To interrogate the effects of device stiffness on the mechanics of an epithelium under tension, we used the medium and high nominal tensile stiffness (k_T) devices. We brought the two cell adhesion planks together, delivered approximately 2700 MDCK Ecad:DsRed cells, and allowed them to form an epithelium for 18 h. We displaced the actuating plank by 50 μm in tension in a single step, and the movement of the sensing plank was observed in order to calculate the force experienced by the epithelium over time (figure 8(a)). Each device was re-used to perform three independent experiments. The epithelial force was calculated every 0.5 min for 30 min following the application of mechanical perturbation (figure 8(b)). The

mean of the three experiments at each time point is denoted by a cross, and the gray bars represent the range of the results. In each experiment, we measured the maximum tensile force (F_{T-MAX}) and the 63% τ time constant (τ_T), and compiled them based on device stiffness (figure 8(c)). We measured a higher F_{T-MAX} when the stiffness of the device was higher ($p < 0.05$). This force decayed more quickly when we used the stiffer device ($p < 0.05$). All statistical tests were Mann–Whitney U.

While the range of nominal tensile spring constants in the low, medium, and high k_T devices spans an order of magnitude, in practice, we conducted all experiments with the 8 μm (medium) and 11 μm (high) devices, as the 5 μm (low) devices exhibited compromised durability. By using a series of devices with varying tensile stiffness, we could probe the effects of different device stiffnesses on the mechanics of an epithelium. The single-step displacement and the 30 min observation window are too short to capture the dynamics of cell motility. Therefore, the differences in the measured response are likely to be primarily mechanical. In fact, the maximum force results match the characteristic response of viscoelastic material, where the resistance of the material is larger following a more rapid application of force, which would be the case using a stiffer device. Following this instantaneous maximum force, the epithelium deformed more rapidly with the characteristic exponential decay of a viscoelastic material. In this study, this device and its integration with live cell microscopy allowed us to probe the viscoelastic properties of the epithelium in tension in the short term, while in a previous study, we probed the cell motility response of the epithelium over a longer time (Sadeghipour *et al* 2018).

4.2. Cyclic shear loading

To interrogate the effects of device stiffness and cyclic loading on the mechanics of an epithelium under shear, we used the medium and high nominal shear stiffnesses (k_S) devices; cells were seeded in the same manner as for tensile testing. We then displaced the actuating plank by 100 μm in the X direction in three alternating steps at times 0, 30, and 60 min, and observed the movement of the sensing plank to calculate the force experienced by the epithelium over time (figure 9(a)). The first step shear at time 0 min allowed us to directly compare these results with the tension experiments, and the subsequent shear steps enabled the first study of the effects of cyclic shear on an epithelium.

We performed three independent experiments with each device type and calculated the epithelium force every 0.5 min for a total period of 90 min (figure 9(b)). As before, the cross represents the mean of the three experiments at each time point, and the gray bars represent the range of the results. For each perturbation, we calculated the magnitude of the maximum shear force ($|F_{S-MAX}|$, figure 9(c)) and the 63% time constant (τ_S, figure 9(d)), and compiled them based on device stiffness and position in the shear sequence. Neither increasing the shear stiffness of the device, nor cyclic loading of the epithelium led to statistically significant changes in $|F_{S-MAX}|$ (figure 9(c)). Increasing device stiffness, k_S, led to a decreased τ_S for the 1st and 3rd shear perturbations ($p < 0.05$), but no statistically significant change in τ_S for the 2nd perturbation (figure 9(d)). The decrease in the 2nd perturbation (figure 9(d)). The decrease in τ_S with increasing k_S was consistent with the results observed in the tension experiments. However, cyclic loading of the epithelium, per

k_S, decreased τ_S ($p < 0.05$, figure 9(d)). Epithelia can reinforce their adhesion and stiffen in response to external stimuli (Ladoux and Mege 2017), thus the fact that cyclic loading led to a decrease in τ_S suggests that the epithelium lost its ability to resist shear loading over multiple perturbations.

5.   Discussion and conclusions

We have successfully designed, modeled and fabricated silicon sensing and actuating devices for the application of shear and tension to a micro-tissue. We integrated this device with live cell fluorescent imaging to mechanically perturb, and image an MDCK epithelium over multiple hours. Interestingly, unlike in tension ($|F_{T-MAX}|$, figure 8(c)), we did not measure a statistically significant change in the maximum shear force for different device stiffnesses ($|F_{S-MAX}|$, figure 9(c)). Our results suggest that different molecular and cellular structures are involved in resisting tension and shear in epithelia. We previously showed that inhibiting actin-myosin contraction in MDCK cells resulted a faster force relaxation after shear (Sadeghipour *et al* 2018). Although in a different cell type, Luo *et al* 2013 found that certain actin crosslinkers respond to different types of cell deformations. Particularly, that filamin accumulated in regions of cellular shear deformation. Molecular crosslinking of filamin to actin changes the mechanical network of the cytoskeleton at a cellular level, which could alter the mechanical response of an epithelial monolayer. It would be interesting to determine if filamin, along with actin-myosin contractions, are responsible for the resistive forces we see in our cyclic shear experiments of epithelial cell monolayers.

The epithelia exhibited a characteristic exponential force relaxation in both tension and shear, which suggests a viscoelastic response in both cases. In cyclic shear loading, we did not measure a change in $|F_{S-MAX}|$ but we did measure a reduced resistance to shear, τ_S, after the second shear. The epithelium would have had enough time to begin reorienting its cytoskeletal structures to account for these stresses in the hour that elapsed between the application of the first and the third shear perturbations. In future work, increasing the number of shear perturbations may reveal a change in $|F_{S-MAX}|$. One prediction is that multiple shears at the same 30 min interval could elicit a monolayer response that adapts to resist shear, resulting in a higher $|F_{S-MAX}|$. Additionally, decreasing the interval of shear may not give the cell monolayer enough time to rearrange molecular structures in order to resist multiple shears thus resulting in decreased $|F_{S-MAX}|$ per increasing shear perturbation. Performing additional experiments with this device in conjunction with cells expressing fluorescently-tagged cytoskeletal structures, such as F-actin, or with targeted pharmaceutical perturbations to depolymerize or stabilize the cytoskeleton would enable dissection of pathways involved in resisting tension versus shear.

Acknowledgments

References

Ayón AA. 1999; Characterization of a time multiplexed inductively coupled plasma etcher. J. Electrochem. Soc. 146 :339.

Barlian AA, Park S-J, Mukundan V and Pruitt BL 2007 Design and characterization of microfabricated piezoresistive floating element-based shear stress sensors Sensors Actuators A 134 77–87

Borghi N, Sorokina M, Shcherbakova OG, Weis WI, Pruitt BL, Nelson WJ and Dunn AR 2012 E-cadherin is under constitutive actomyosin-generated tension that is increased at cell-cell contacts upon externally applied stretch Proc. Natl Acad. Sci. USA 109 12568–73 [PubMed: 22802638]

Doll JC and Pruitt BL 2012 High bandwidth piezoresistive force probes with integrated thermal actuation J. Micromech. Microeng 22 095012 [PubMed: 23175616]

Harris AK, Wild P and Stopak D 1980 Silicone rubber substrata: a new wrinkle in the study of cell locomotion Science 208 177–9 [PubMed: 6987736]

Higgs GC, Simmons CS, Gao Y, Fried A, Park SJ, Chung C and Pruitt BL 2013 MEMS-based shear characterization of soft hydrated samples J. Micromech. Microeng 23 085001

Holman JP19946th editionExperimental Methods for Engineers Vol. (New York: McGraw-Hill)

Hopcroft MA, Nix WD and Kenny TW 2010 What is the young's modulus of silicon? J. Microelectromech. Syst 19 229–38

Hui J and Pang SW 2019 Cell migration on microposts with surface coating and confinement Biosci. Rep 39 BSR20181596 [PubMed: 30674640]

Kaajakari V2009Practical MEMS (Las Vegas, NV: Small Gear)

Kim K, Taylor R, Sim JY, Park J, Norman J, Fajardo G, Bernstein D and Pruitt BL 2011 Calibrated micropost arrays for biomechanical characterisation of cardiomyocytes Micro Nano Lett. 6 317–22

Ladoux B and Mege RM 2017 Mechanobiology of collective cell behaviours Nat. Rev. Mol. Cell Biol 18 743–57 [PubMed: 29115298]

Langlois ED, Shaw GA, Kramar JA, Pratt JR and Hurley DC 2007 Spring constant calibration of atomic force microscopy cantilevers with a piezosensor transfer standard Rev. Sci. Instrum 78 093705 [PubMed: 17902953]

Lee S, Mandic J and Van Vliet KJ 2007 Chemomechanical mapping of ligand-receptor binding kinetics on cells Proc. Natl Acad. Sci. USA 104 9609–14 [PubMed: 17535923]

Luo T, Mohan K, Iglesias PA and Robinson DN 2013 Molecular mechanisms of cellular mechanosensing Nat. Mater 12 1064–71 [PubMed: 24141449]

Maitre JL, Berthoumieux H, Krens SF, Salbreux G, Julicher F, Paluch E and Heisenberg CP 2012 Adhesion functions in cell sorting by mechanically coupling the cortices of adhering cells Science 338 253–6 [PubMed: 22923438]

Mukundan V, Nelson WJ and Pruitt BL 2013 Microactuator device for integrated measurement of epithelium mechanics Biomed. Microdevices 15 117–23 [PubMed: 22927158]

Mukundan V, Ponce P, Butterfield HE and Pruitt BL 2009 Modeling and characterization of electrostatic comb-drive actuators in conducting liquid media J. Micromech. Microeng 19 1–9

Petzold BC, Park SJ, Ponce P, Roozeboom C, Powell C, Goodman MB and Pruitt BL 2011 Caenorhabditis elegans body mechanics are regulated by body wall muscle tone Biophys. J 100 1977–85 [PubMed: 21504734]

Plotnikov SV, Sabass B, Schwarz US and Waterman CM 2014 High-resolution traction force microscopy Methods Cell Biol. 123 367–94 [PubMed: 24974038]

Ribeiro AJ, Denisin AK, Wilson RE and Pruitt BL 2016 For whom the cells pull: hydrogel and micropost devices for measuring traction forces Methods 94 51–64 [PubMed: 26265073]

Roca-Cusachs P, Conte V and Trepat X 2017 Quantifying forces in cell biology Nat. Cell Biol 19 742–51 [PubMed: 28628082]

Sadeghipour E. et al. 2018; Shear-induced damped oscillations in an epithelium depend on actomyosin contraction and E-cadherin cell adhesion. eLife. 7 :e39640. [PubMed: 30427775]

Siechen S, Yang S, Fau - Chiba A, Chiba A, Fau - Saif T and Saif T 2009 Mechanical tension contributes to clustering of neurotransmitter vesicles at presynaptic terminals Proceedings of the National Academy od Sciences 106 12611–12616

Sochol RD, Higa AT, Janairo RRR, Li S and Lin L 2011 Effects of micropost spacing and stiffness on cell motility Micro Nano Lett. 6 323–6

Sun Y, Nelson BJ, Potasek DP and Enikov E 2002 A bulk microfabricated multi-axis capacitive cellular force sensor using transverse comb drives J. Micromech. Microeng 12 832–40

Taubenberger AV, Hutmacher DW and Muller DJ 2014 Single-cell force spectroscopy, an emerging tool to quantify cell adhesion to biomaterials Tissue Eng. B 20 40–55
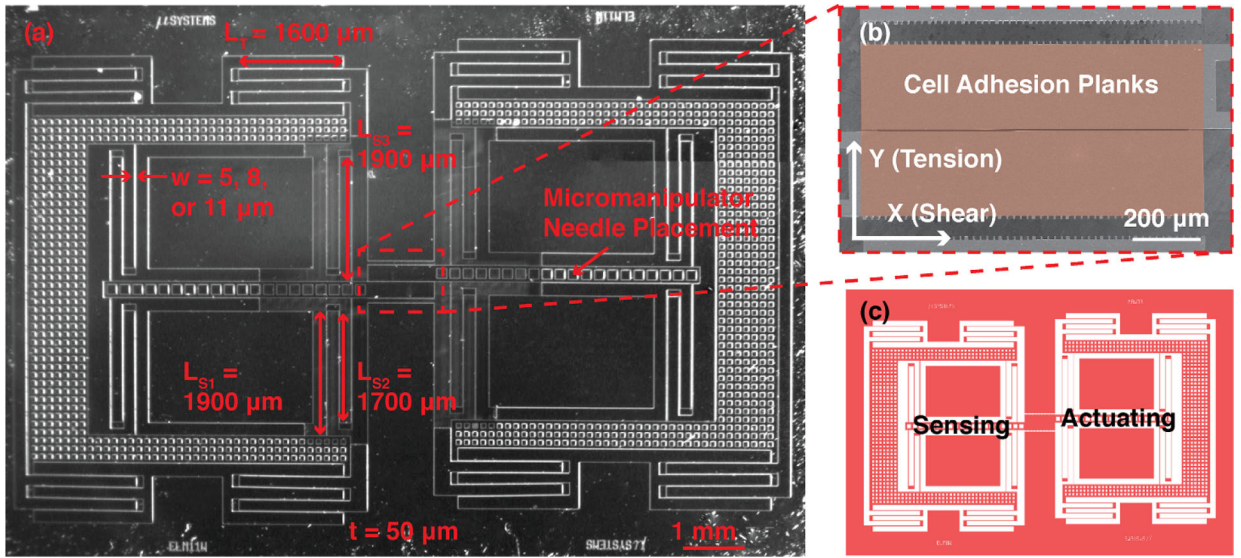
Figure 1.
Folded flexures placed in parallel suspend the cell adhesion planks of the cell mechanics device.(a) The silicon die (8.5 × 12.4 mm) features two cell culture regions or 'planks,' each suspended by four symmetric sets of folded flexures to provide compliance in Y, and another four sets to provide compliance in X. The Y (tension) stiffness of the device is defined by dimensions (L_T, w, and t) of the tension beams, and the X (shear) stiffness of the device is defined by dimensions (L_{S1}, L_{S2}, L_{S3}, w, and t) of the shear beams (L: Length, w: width, t: thickness). (b) These flexures enable relative motion of the planks to apply tension or shear to an adhered cell monolayer, where the force across the monolayer may be calculated based on the spring stiffness in each direction. (c) All of the moving components (actuating and sensing) of the device are defined by a single lithographic mask.
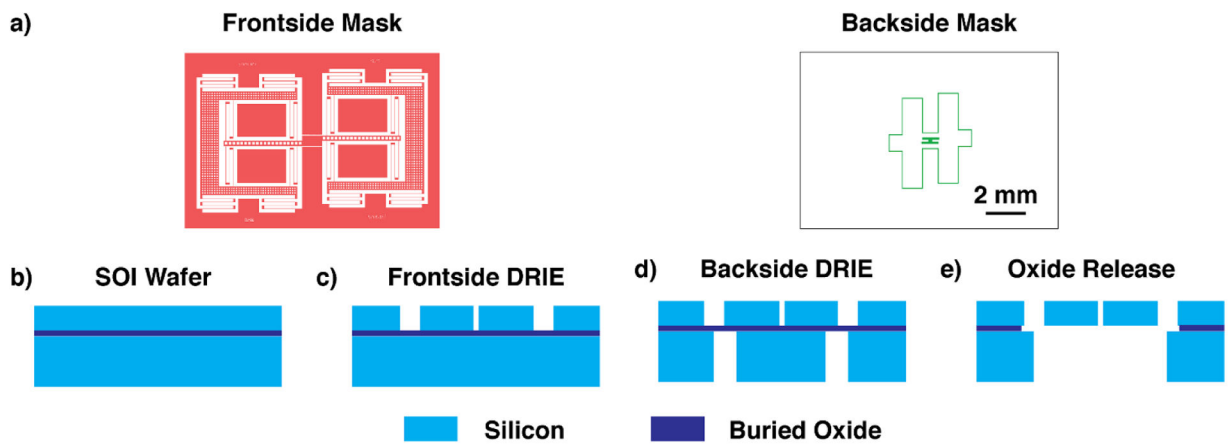
Figure 2.
The devices are defined by two lithography steps, and frontside and backside DRIE. (a)
Frontside etch mask layout and backside etch mask layout. (b) Anneal SOI to release built-in
stress in the buried oxide. (c) Define frontside structures using a DRIE process. (d) Define
backside release areas under moving structures and flexures using a DRIE process. (e)
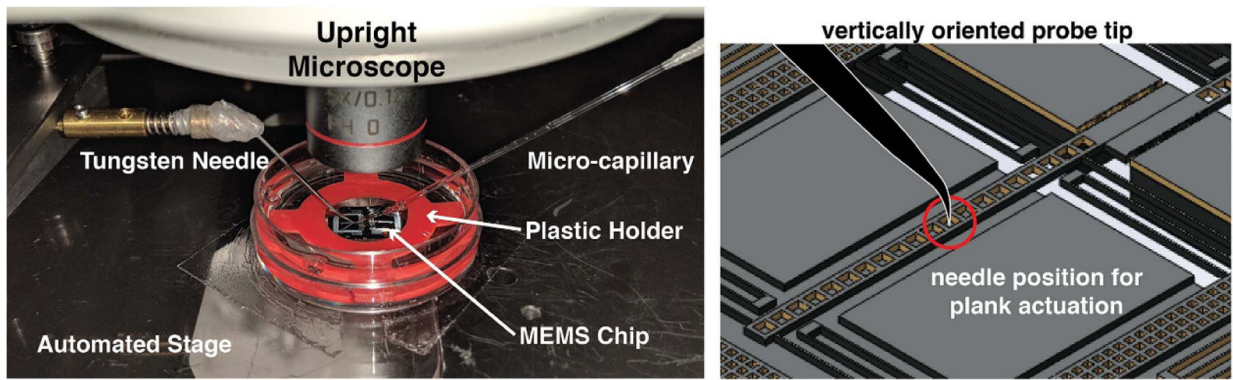Release the moving structures by etching the BOX in BOE.

Figure 3.
Mounting the device in an open cell culture dish allows access for a micromanipulator needle and an immersion microscope objective. Left; Device is positioned using a custom 3D-printed plastic holder (red). The open culture dish is adhered with double sided tape to an upright microscope (Leica DMRXA2) stage. A three-axis micromanipulator and tungsten needle move the actuating plank in the x and/or y direction. Another three-axis micromanipulator and pipette with a micro-capillary deposit cells on the silicon planks. **Right:** schematic depicts the vertical orientation of the tungsten needle probe tip and its position of contact for plank actuation.
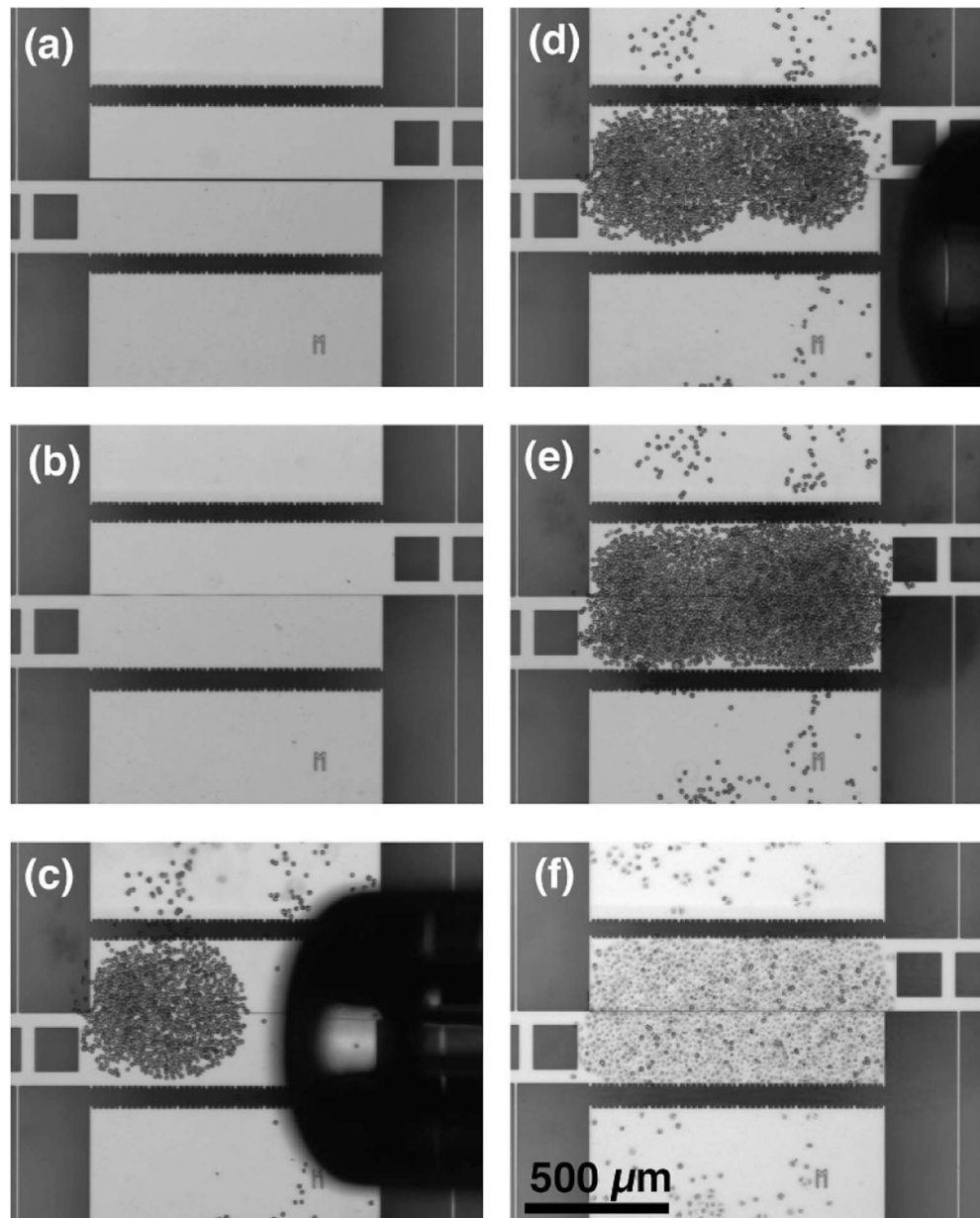
Figure 4.
Placing a controlled cell population enables reproducible experiments and minimizes
potential for interference in the flexure regions.(a–b) The actuation plank (top) is moved
5 μm in tension to close the gap to the sensing plank (bottom). (c–e) E-cadherin:dsRed
MDCK cells are delivered In three steps (~900 cells each) using a micro-capillary tube. (f)
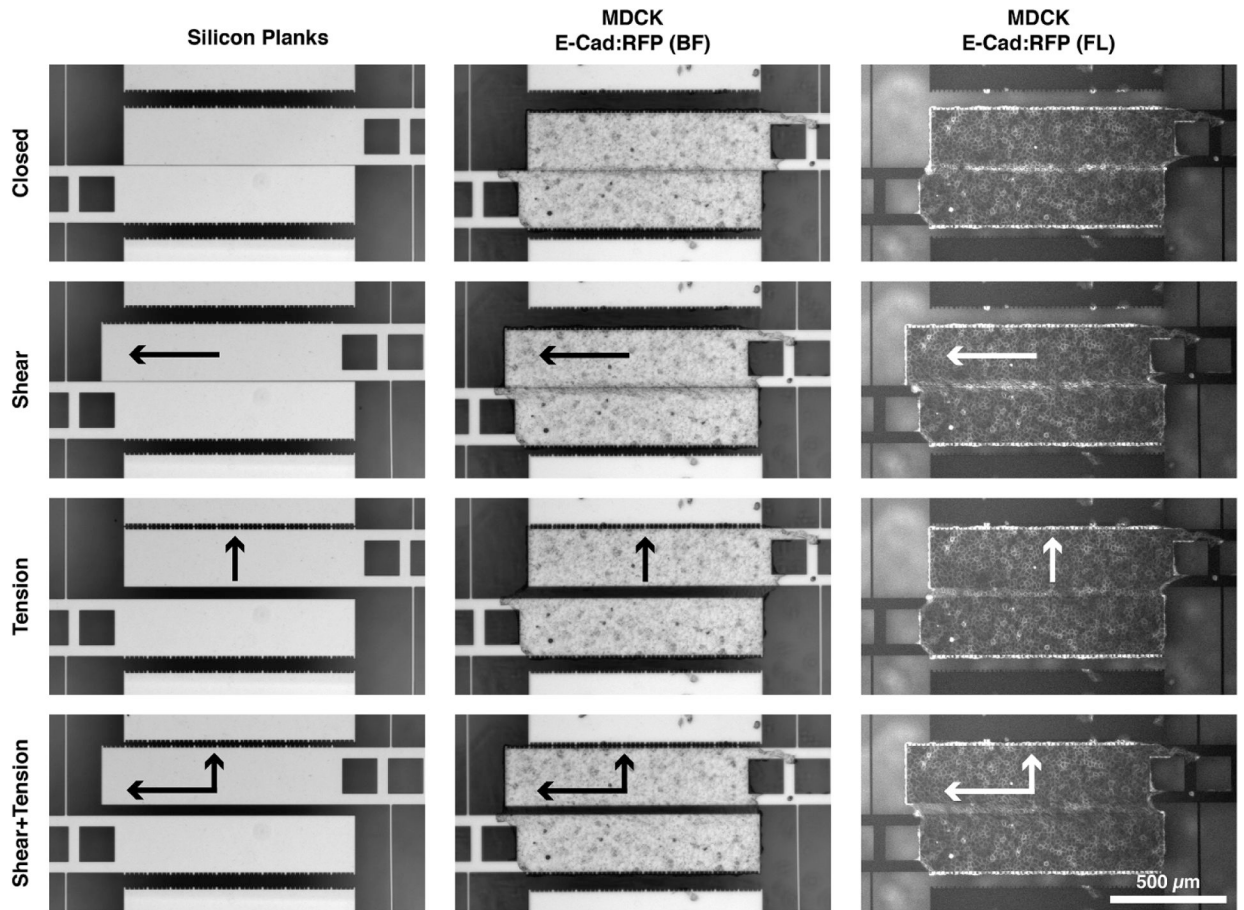MDCK cells form a monolayer across both planks 3 h after cell seeding.

Figure 5.
The epithelial monolayer stays intact over the full range of tensile and shear motion used in the experiments.
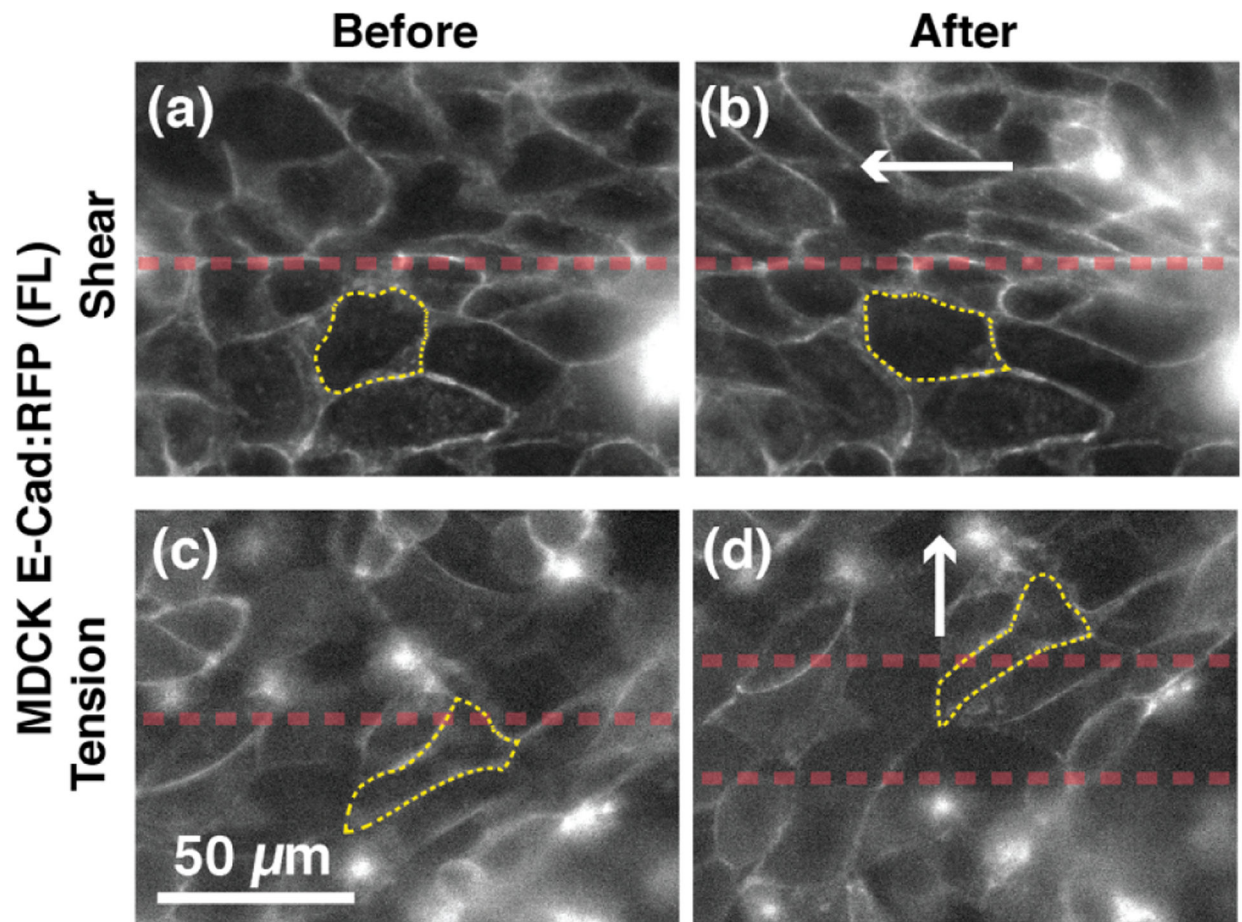
Figure 6.
Cells adjacent to the area of stress application deform and change aspect ratio.(a and c) MDCK E-cadherin:dsRed cells before shear (a) or tension (c). (b) Application of 100 μm displacement in shear. (d) Application of 50 μm displacement in tension. Individual cell boundaries were defined through fluorescent imaging of E-cadherin:dsRed MDCK cells.
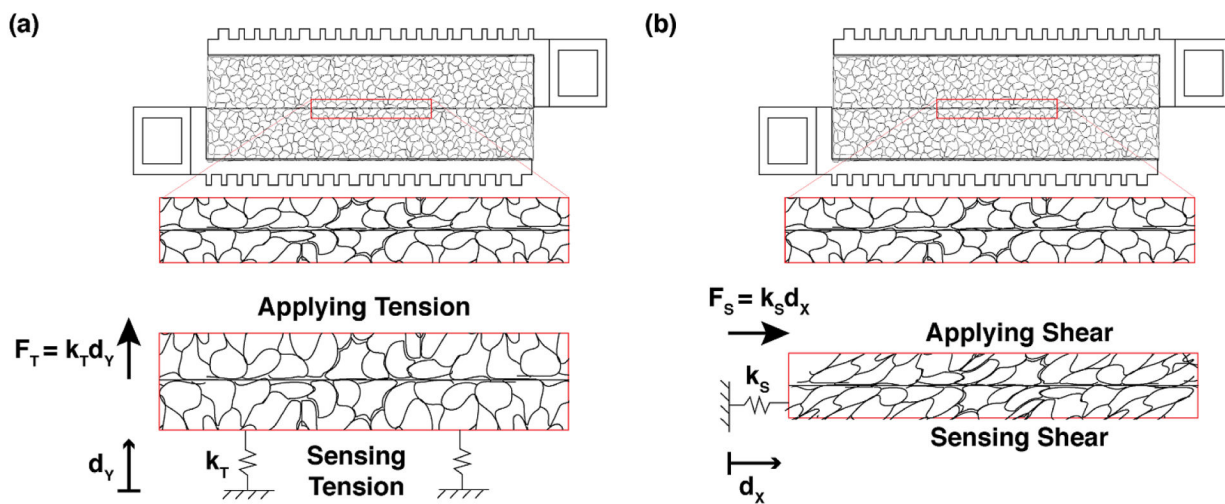
Figure 7.
Tensile and shear forces on epithelium are calculated using spring stiffnesses and displacements in Y and X, respectively.(a) The tensile force (F_T) on the epithelium is the product of the tensile spring stiffness (k_T) and the Y displacement (d_Y), measured optically. (b) The shear force (F_S) on the epithelium is the product of the shear spring stiffness (k_S) and the X displacement (d_X), measured optically.
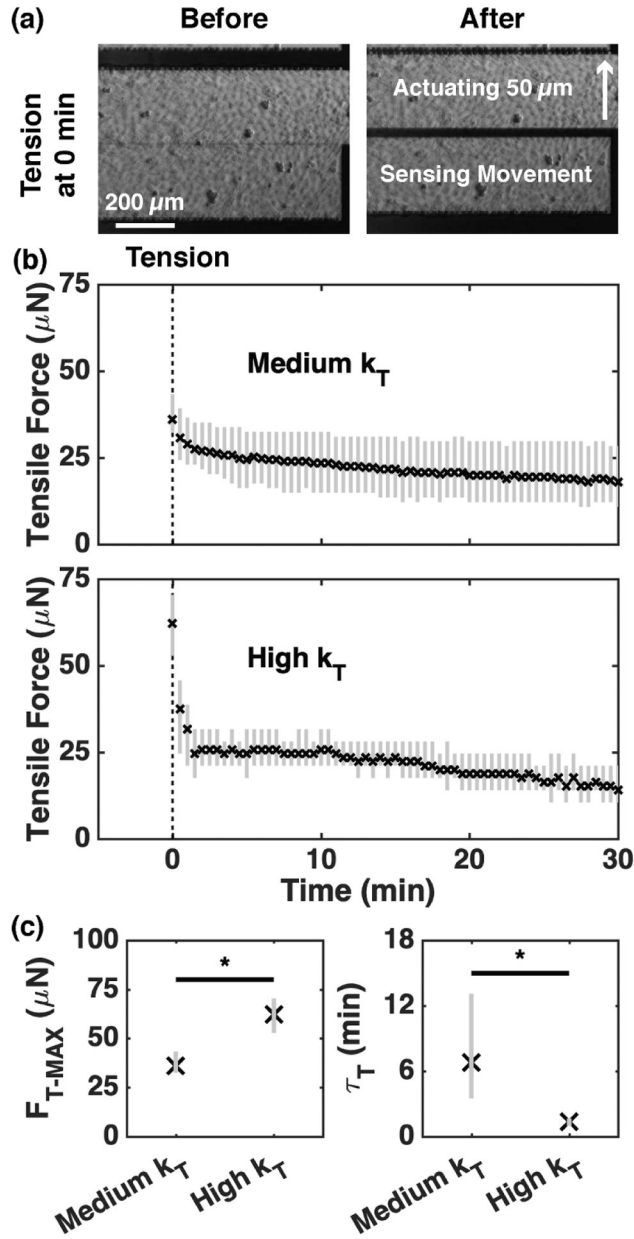
Figure 8.
MDCK epithelium under tension in stiffer device exhibits higher maximum tensile force (F_{T-MAX}) and faster tensile force relaxation (τ_T). (a) MDCK epithelium before (left) and after (right) the application of 50 μm tensile displacement. (b) The range (solid gray line) and mean (cross) of the measured resistive force of an epithelium (three independent experiments) over 30 min (every 0.5 min) after perturbation (dashed black line) using devices with medium (top) and high (bottom) nominal tensile stiffness (k_T). (c) Higher k_T increases F_{T-MAX} and decreases τ_T ('*': $p < 0.05$, Mann–Whitney U).
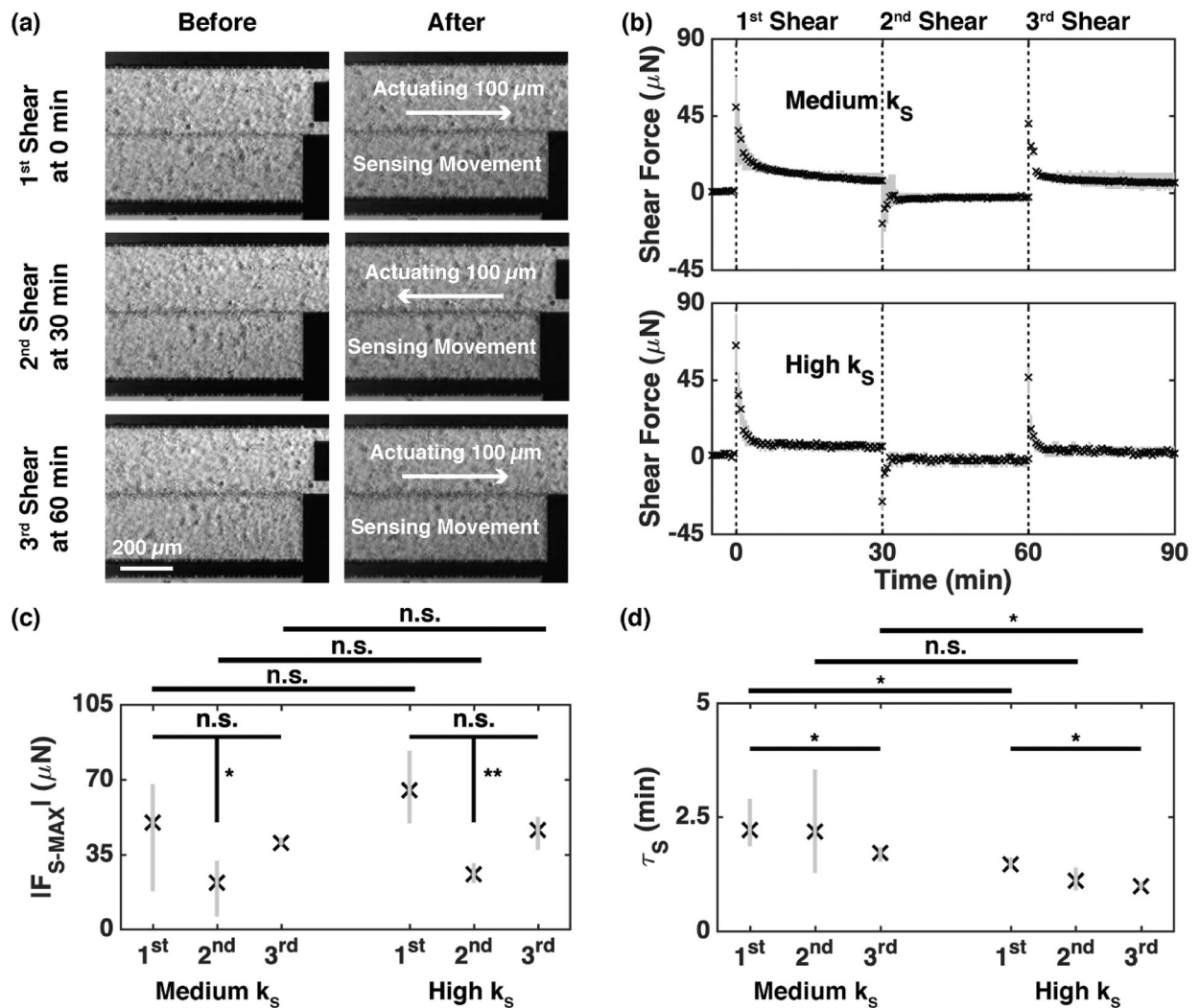
Figure 9.
MDCK epithelium under cyclic shear exhibits no change in magnitude of maximum shear force |F_{S-MAX}|, but shows faster shear force relaxation (τ_S). (c) MDCK epithelium before (left) and after (right) application of 100 μm cyclic shear displacement, at 0 (top), 30 (middle), and 60 min (bottom). (b) The range (solid gray line) and mean (cross) of the measured resistive force of an epithelium (three independent experiments) over 90 min (every 0.5 min) after perturbations (dashed black lines) at times 0, 30, and 60 min, using devices with medium (top) and high (bottom) nominal shear stiffness (k_S). (c) Neither changing k_S, nor applying cyclic shear stress changes the magnitude of the maximum shear force (|F_{S-MAX}|, 'n.s.': not statistically significant, Mann–Whitney U). (d) Cyclic shear stress decreases the 63% time constant (τ_S, '*': $p < 0.05$, Mann–Whitney U). In most cases (1st and 3rd shear) increasing k_S decreases τ_S ('*', $p < 0.05$, Mann–Whitney U).

Table 1.

Values for calculating the stiffness of the device in figure 1(a).

Variable	Value
E	169 Gpa
T	50 μm
W	5, 8, or 11 μm
$L_{S1} = L_{S3}$	1900 μm
L_{S2}	1700 μm
L_T	1600 μm

Table 2.

Nominal force resolution using a 10X air (1.54 pixel/μm) objective.

Device Stiffness	w (μm)	Shear		Tension	
		k_S (N m^{-1})	F_{min} (nN)	k_T (N m^{-1})	F_{min} (nN)
Low	5	0.23	149	0.26	169
Medium	8	0.93	604	1.1	714
High	11	2.4	1558	2.7	1753

Table 3.

Device precision for each design.

Device Stiffness	k_S (N m^{-1})		k_T (N m^{-1})	
	Nominal	Range	Nominal	Range
Low	0.23	0.09–0.37	0.26	0.10–0.42
Medium	0.93	0.58–1.28	1.1	0.70–1.50
High	2.4	1.73–3.07	2.7	1.94–3.46